Draft version December 22, 2016
Preprint typeset using LaTeX style AASTeX6 v. 1.0

arXiv:1612.07008v1 [astro-ph.EP] 21 Dec 2016

A FRAMEWORK TO COMBINE LOW- AND HIGH-RESOLUTION SPECTROSCOPY FOR THE ATMOSPHERES OF TRANSITING EXOPLANETS

M. Brogi[1,6], M. Line[2], J. Bean[3], J.-M. Désert[4], and H. Schwarz[5]

[1]Center for Astrophysics and Space Astronomy, University of Colorado at Boulder, Boulder, CO 80309, USA
[2]School of Earth and Space Exploration, Arizona State University, Tempe, AZ 85287, USA
[3]Department of Astronomy & Astrophysics, University of Chicago, 5640 S Ellis Ave, Chicago, IL 60637, USA
[4]Anton Pannekoek Institute for Astronomy, University of Amsterdam, 1090 GE Amsterdam, The Netherlands
[5]Leiden Observatory, Leiden University, Postbus 9513, 2300 RA Leiden, The Netherlands
[6]NASA Hubble Fellow

ABSTRACT

Current observations of the atmospheres of close-in exoplanets are predominantly obtained with two techniques: low-resolution spectroscopy with space telescopes and high-resolution spectroscopy from the ground. Although the observables delivered by the two methods are in principle highly complementary, no attempt has ever been made to combine them, perhaps due to the different modeling approaches that are typically used in their interpretation. Here we present the first combined analysis of previously-published dayside spectra of the exoplanet HD 209458 b obtained at low resolution with HST/WFC3 and Spitzer/IRAC, and at high resolution with VLT/CRIRES. By utilizing a novel retrieval algorithm capable of computing the joint probability distribution of low- and high-resolution spectra, we obtain tight constraints on the chemical composition of the planet's atmosphere. We measure a metallicity 0.1-3.7× the stellar value (1σ) and our analysis strongly favors an oxygen-rich atmosphere (C/O = $0.43^{+0.04}_{-0.06}$). While the abundance of H_2O is consistent with the expectations for a solar-composition atmosphere in chemical equilibrium, CO is found slightly under-abundant (1.9σ) and CO_2 over-abundant (2.2σ). This study opens the way to coordinated exoplanet surveys between the flagship ground- and space-based facilities, which ultimately will be crucial for characterizing potentially-habitable planets.

Keywords: methods: data analysis — planets and satellites: atmospheres — techniques: spectroscopic

1. INTRODUCTION

Nearly fifteen years of observations with photometry and Low-Dispersion Spectroscopy (LDS) have significantly advanced our understanding of exoplanet atmospheres (e.g., Sing et al. 2016). In particular, the Hubble Wide Field Camera 3 (WFC3) has produced robust and repeatable observations, resulting in physically sensible atmospheric composition interpretations. Its band around 1.4 μm has a strong diagnostic power since it targets major sources of opacity for exoplanet atmospheres (primarily H_2O, but also CH_4, HCN, and NH_3). The interpretation of LDS data is also supported by state-of-the art retrieval algorithms (e.g., Madhusudhan & Seager 2011; Benneke & Seager 2012; Line et al. 2013; Waldmann et al. 2015). When multiple species overlap, however, ambiguities arise in molecular identification and abundance determinations.

High-Dispersion spectroscopy (HDS) from the ground has recently emerged as an additional tool to characterize exoplanet atmospheres (e.g., Snellen et al. 2010, 2014; Brogi et al. 2012). HDS is able to distinctly determine the presence of specific molecular species, despite overlap. For emission spectra, absorption and emission are intrinsically discriminated, allowing the direct detection of thermal inversion layers. Due to the large opacity difference between the core and the wings of molecular lines, HDS probes a broad range in atmospheric temperatures and pressures. However, retrieving atmospheric properties (especially absolute molecular abundances) from HDS data is challenging. This is partly due to the loss of the planet+star continuum from self-calibration of the data, and additionally to the lack of robust retrieval algorithms. Inference in HDS data analysis is naturally done through forward modeling, since atmospheric signatures are searched by cross-correlating with template spectra, which combines the signal of tens or hundreds of molecular lines. Not only is this process computationally cumbersome, but also the statistical properties of the resulting cross-correlation functions (CCFs) are far from trivial.

In this paper we present a novel analysis technique to combine the strengths of high-resolution and low-resolution spectroscopy. We demonstrate the method on dayside spectroscopic observations of the hot Jupiter HD 209458 b (Henry et al. 2000; Charbonneau et al. 2000). As one of the best-characterized transiting exoplanets, it is the ideal target for testing our new method. We aim to show that, when combining LDS and HDS, the sensitivity to a wider range in atmospheric pressures and the ability of HDS to disentangle overlapping molecular features can significantly improve the inference of the chemical compositions of exoplanet atmospheres.

2. OBSERVATIONS AND REANALYSIS OF CRIRES SPECTRA

The LDS dataset used for this work is described in Line et al. (2016) and shown in Figure 1. It consists of eclipse observations of HD 209458 b obtained with Hubble/WFC3 in the range 1.125-1.655 μm, and with Spitzer/IRAC at 3.6, 4.5, 5.8, and 8.0 μm from Diamond-Lowe et al. (2014).

The HDS data consist of two half nights of dayside spectra taken with VLT/CRIRES in the range 2.287-2.345 μm at a resolution of 100,000, and are described in detail in Schwarz et al. (2015). We only include the nodded observations (2 out of 3 sets of data) for which we have a good understanding of the instrument. We utilize the same calibrated and extracted spectra as Schwarz et al. (2015), but one important difference in our current analysis is that we also estimate the weight of each CRIRES detector based on the injection and retrieval of an artificial signal. This is the best-fitting, CO-only model spectrum of Schwarz et al. (2015), scaled via

$$F_{\rm scaled}(\lambda) = \frac{F_{\rm model}(\lambda)}{B(\lambda, T_{\rm B})} \left(\frac{R_{\rm P}}{R_{\rm S}}\right)^2, \qquad (1)$$

where $R_{\rm P}$ and $R_{\rm S}$ are the planet and stellar radii, respectively, and B is the Planck function at temperature $T_{\rm B} = 6300$ K, which matches the continuum of HD 209458 around 2.3 μm. The scaled model is Doppler-shifted to the planet radial velocity computed with a semi-amplitude of $K_{\rm P} = (145.9 \pm 2.4)$ km s^{-1}, i.e., the value obtained from the literature (Knutson et al. 2007; Torres et al. 2008), assuming a circular orbit.

The scaled and shifted model is injected in the data at 5× the nominal level via

$$F_{\rm inj}(t, \lambda) = F_{\rm obs}(t, \lambda)[1 + 5F_{\rm scaled}(t, \lambda)], \qquad (2)$$

A scaling factor of 5 is the minimum required to achieve a S/N≥3 in all of the four detectors. The model is injected as early as possible in the analysis, i.e., after the spectra are aligned to the common telluric reference frame. We then remove telluric lines and cross correlate the residual spectra with the model as in Brogi et al. (2012, 2014). The injected artificial signal is retrieved by co-adding the CCFs from each night and each CRIRES detector at the planet radial velocity. We find that all four CRIRES detectors contain significant signal, but their relative weight differs between nights and between detectors, possibly due to varying observing conditions and the unequal density of CO spectral lines with wavelength. When weighting the CCFs between the observed spectra and the model by the square of the measured artificial S/N (i.e., the peak value of the CCF divided by the r.m.s. of the noise), the tentative detection of Schwarz et al. (2015) becomes a solid detection of CO in absorption at S/N=5.3. We do not proceed to explore the full model grid of Schwarz et al. (2015) at this stage, but we utilize the weighting and the analysis described above to test a novel retrieval method.

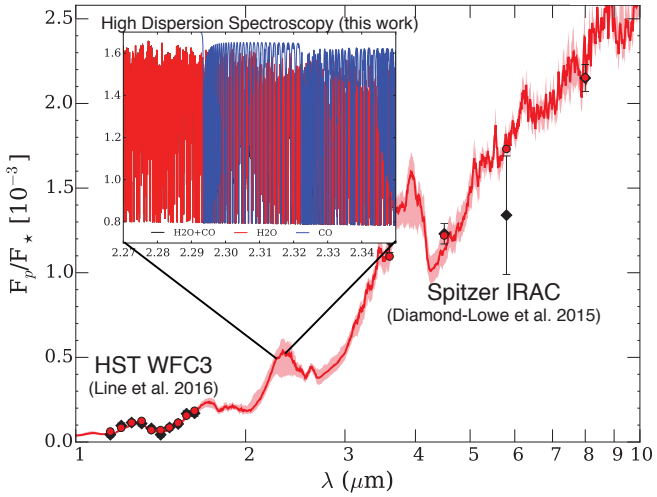

Figure 1. Dayside spectrum of HD 209458 b, with LDS data (WFC3+Spitzer) plotted with black diamonds. Over-plotted in red is the best-fitting low-resolution model spectrum and its 1-σ uncertainty. The inset shows the best-fitting HDS model based on this analysis and fitted to CRIRES 2.3-μm data.

3. JOINT LDS+HDS ANALYSIS

Our aim is to combine the complementary information from LDS and HDS and compute a joint posterior distribution. LDS data can be compared to models in a straightforward manner (e.g., via "chi-square"), whereas the signal in HDS data is extracted by cross-correlating with a family of models. We thus need to define an appropriate metric for quantifying the fit quality of a model to HDS data. Since comparing models via cross correlation is computationally expensive, we also need to design an efficient exploration of the parameter space.

3.1. *A metric for the fit quality of high-resolution model spectra*

The cross-correlation function between the data and a model is maximized when both the position and the strength of spectral lines *relative* to each other match. However, due to invariance under scaling, maximizing the cross-correlation signal is not equivalent to matching the *absolute* line-to-continuum contrast. This additional constraint can be fulfilled by minimizing the residual cross-correlation signal when each model is subtracted from the data. In other words, the best-fitting model will maximize the cross correlation with the observed spectra and minimize the cross correlation with the model-subtracted data. These two requirements are incorporated into a consistent statistical framework adapted from Brogi et al. (2016):

- The model is directly cross-correlated with the data after telluric lines are removed[1]. No match would produce a distribution of cross-correlation values consistent with random noise, i.e., with a flat line. The deviation from a flat line therefore indicates that a signal of some kind is detected. This is quantified by computing the χ^2 of the cross correlation values around the planet radial velocity ($\chi^2_{\rm dir}$). The probability of measuring $\chi^2_{\rm dir}$ given n degrees of freedom $P(\chi^2_{\rm dir}, n)$ is computed and translated into a sigma value $\sigma_{\rm dir}$ for a Normal distribution with a two-tail test. A range of planet radial-velocity semi-amplitudes $K_{\rm P}$ within 4σ from the literature value is explored;

- The model is scaled to the observed planet/star flux ratio based on Eq. 2, Doppler shifted based on the same range of $K_{\rm P}$ indicated above, and subtracted from the data via Eq. 1, with scaling factor -1. Telluric lines are again removed and the residuals cross correlated with the model. A perfect match between the planet signal and the scaled model will result in a perfect subtraction. Therefore the cross-correlation function of the residuals will be consistent with random noise, which means its sigma value $\sigma_{\rm sub}$ computed as above from the chi square $\chi^2_{\rm sub}$ of cross-correlation values will be approximately zero;

- The best-fitting model is found by maximizing the difference $\Delta\sigma = \sigma_{\rm dir} - \sigma_{\rm sub}$. In this study this is equivalent to maximizing the $\Delta\chi^2 = \chi^2_{\rm dir} - \chi^2_{\rm sub}$, but this formulation is more general, as it allows us to test additional parameters when subtracting the model, e.g., line broadening due to rotation as in Brogi et al. (2016). It only requires adjusting the degrees of freedom n when computing $P(\chi^2, n)$.

[1] Stellar lines are negligible at the effective temperature of HD 209458, and weak lines are effectively removed together with telluric lines

3.2. *Exploring the HDS parameter space*

The algorithm outlined in Section 3.1 runs in approximately 4 minutes per model on a single core of a modern UNIX machine. It is therefore computationally too expensive to run a full MCMC for the HDS data that would include 10^5-10^6 models. However, since our final goal is to produce the *joint* posterior distribution of LDS and HDS data combined, we can neglect regions of the parameter space which are already strongly disfavored by the LDS analysis. This is done by feeding the HDS analysis with a set of models sampled from the LDS posterior distribution of Line et al. (2016). The parametrization consists of molecular abundances for 7 species (CO, H_2O, CH_4, CO_2, C_2H_2, NH_3, HCN) and five additional parameters to sample the temperature-pressure profile as in Parmenter & Guillot (2014). The 12-dimensional LDS posterior is sampled with 5,000 points, and the corresponding high-resolution, disk-integrated emission spectra are computed via line-by-line radiative-transfer calculations with the CHIMERA (Line et al. 2013, 2014, 2015) emission forward model. Examples of LDS and HDS model spectra are shown in Figure 1.

We use the absorption cross-section database (and references there-in) from Freedman et al. (2008) with subsequent upgrades described in Freedman et al. (2014). The database comprises pre-computed cross-sections on a grid of temperature and pressure points sampled at intervals of 0.01 $\rm cm^{-1}$. This corresponds to a resolution $R \sim 430,000$, enough to resolve the individual lines (e.g., resolve the half-widths) at the CRIRES wavelengths over the physically relevant ranges of temperatures and pressures[2]. The opacity sources include H_2-H_2/He collision induced absorption, and molecular absorption due to the seven species listed above. Note these are the same opacities used for the LDS data retrieval in Line et al. (2016).

3.3. *Computing the joint posterior*

We compute the significance of the high-resolution models as explained in Section 3.1. To translate this information into an HDS posterior we bin the parameter space by 0.4 in $\log_{10}$(abundance). We then assume that in a posterior-sampling algorithm such as a MCMC, a model n-σ deviant from the best-fitting model would

[2] We also experimented with higher-resolution (0.001 $\rm cm^{-1}$) tabulated cross-sections computed with the HITRAN HAPI module and the HITEMP database, and found negligible differences between the lines sampled at 0.01 $\rm cm^{-1}$ and 0.001 $\rm cm^{-1}$ grid resolutions.

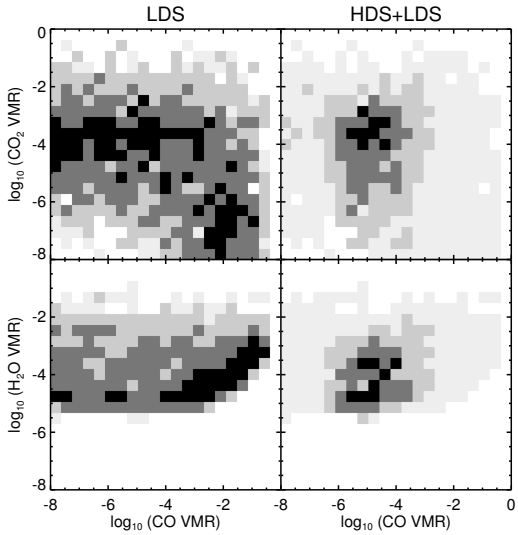

Figure 2. Example of combined LDS and HDS analysis. The log(abundance) of carbon monoxide is plotted against that of water vapor and carbon dioxide. The 1-σ, 2-σ, 3-σ, and >3σ confidence intervals are plotted in greyscale (from black to light grey). For these three species the joint posterior results in much tighter constraints on the molecular abundances.

be extracted with a probability $P = N(n)$, where N denotes a Normal Distribution. As an example, the best-fitting model has $P = 1$ and a model 2-σ deviant $P = 0.046$. The occupancy of a bin in the parameter space is therefore given by the sum of all the probabilities of the models falling in that range. The corresponding histogram is also computed for the LDS posterior. In this case the occupancy is given by the number of models falling in each bin as derived from the LDS retrieval analysis. In order to compute the joint posterior, we multiply the HDS and LDS posterior histograms, bin by bin. This is equivalent to multiplying the probabilities, which means we are treating LDS and HDS as two independent measurements of the same quantities. Figure 2 shows examples of the two-dimensional, LDS (left panels) and LDS+HDS (right panels) posteriors, obtained with the above method. The 1-, 2- and 3-σ confidence intervals are obtained by normalizing the histogram by the total occupancy and cutting the cumulative density function at 61%, 13.5%, and 1.1%, respectively.

Since the HDS posterior is not obtained by freely exploring the parameter space, but it has been conditioned by the LDS analysis, our joint posterior is reliable only when the sampling is sufficiently dense to fill the whole 12-dimensional parameter space, i.e., within the 3-σ confidence interval. This is why in Figure 2 we generically draw in light gray the region of the parameter space more than 3-σ deviant from our best estimate of the parameter, without assigning any further confidence interval. In Section 6 we further discuss the limits of this approach.

4. RESULTS

In Figure 3 we plot the marginalized joint posterior distribution of the 7 species included in our models (in black) and we compare it to their equivalent distribution from the low-resolution data only (in red). In all cases the probability density functions of the joint analysis are narrower, and significantly for H_2O, CO, and CO_2.

The spectral signature of CO is expected to be substantial for giant planets at temperatures greater than 1000 K, and the inclusion of HDS data encompassing a major CO band results in substantially better constraints on its abundance compared to LDS data.

While the abundance of H_2O ($\log_{10}$(VMR)= $-4.1^{+0.3}_{-0.8}$) is found to be consistent with the expectations for a solar-composition atmosphere at the temperature of HD 209458 b, we measure abundances of CO and CO_2 ($\log_{10}$(VMR)= $[-4.9 \pm 0.8, -3.9^{+0.8}_{-1.3}]$, respectively) deviant by -1.9σ and 2.2σ, respectively. CO and CO_2 are both opacity sources in the Spitzer 4.5 μm channel, and their individual abundances cannot be easily disentangled. This is reflected by a broad LDS posterior (Figure 2, left-top panel), which spans a large range of abundances for the two species. However, the inference from the 2.3-μm CRIRES spectra should be unambiguous, as the spectral signatures of CO and CO_2 are disentangled at high spectral resolution. As shown by the top panels of Figure 2, models with relatively low abundance of CO_2 and high CO abundance were tested, and found at least 3-σ deviant from the best-fitting model. We hence tend to exclude a bias from conditioning HDS data with the LDS posterior.

In Figure 4 we show the posterior distribution obtained for the relative abundances of methane, water vapor, and carbon monoxide. The combination of HDS and LDS produces very tight constraints on the relative abundances. For CO and H_2O we measure $\log([CO]/[H_2O]) = -1.1 \pm 0.8$. Relative abundances with methane, which is non-detected, are instead looser as expected, with $\log_{10}([CO]/[CH_4]) = 4.6^{+1.4}_{-2.0}$ and $\log_{10}([H_2O]/[CH_4]) = 5.0 \pm 1.4$.

Assuming chemical equilibrium and a planet temperature of 1700 K, the relative abundances of H_2O and CO alone indicate C/O ≤ 1 at 4.4σ (dashed blue lines in Figure 4). We also compute the C/O by dividing the number densities of C and O atoms derived from their volume mixing ratios. When the number density of carbon dioxide is included, we obtain a very tight estimate of $C/O = 0.43^{+0.04}_{-0.06}$. Without CO_2, the constraint is still consistent but more uncertain ($C/O = 0.76^{+0.14}_{-0.65}$). Both values are consistent with the stellar C/O of 0.46 ± 0.05 (Brewer & Fischer 2016).

We estimate the planet metallicity by assuming H_2/He = 0.193 and deriving the mole fractions of hydrogen

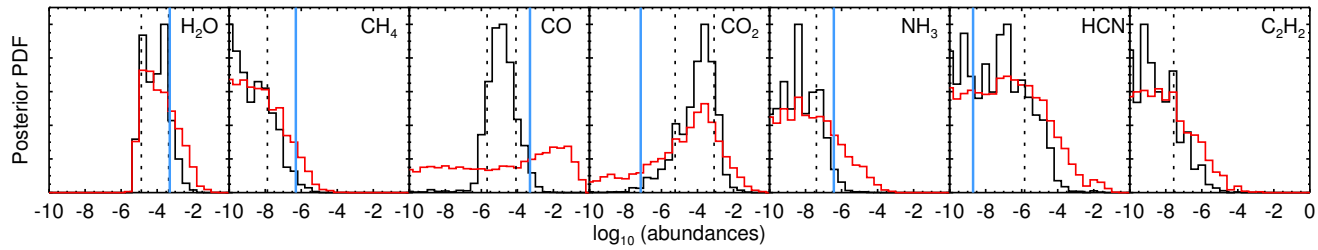

Figure 3. Marginalized probability density function for the abundances of the seven species considered in this study. The LDS posterior (in red) is compared to the joint LDS+HDS posterior (in black). The 15.9-84.1% quantiles are shown with dotted lines, and the values for solar composition and chemical equilibrium with blue solid lines.

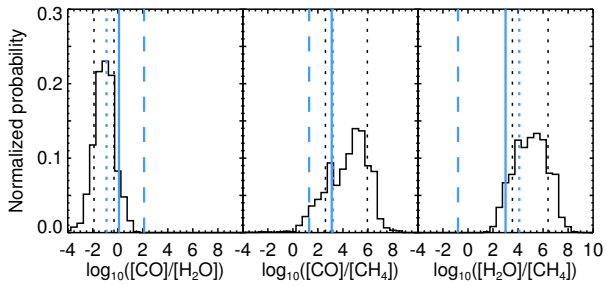

Figure 4. Relative abundances of CO, CH_4, and H_2O as derived from the joint LDS and HDS analysis. The 1-σ confidence intervals for molecular ratios are indicated with black dotted lines. The blue lines show the values expected for C/O=0.5 (solid), C/O=1 (dashed) and C/O=0.1 (dotted). These are computed for chemical equilibrium and a planet temperature of 1700 K (Madhusudhan 2012).

and metals based on their stoichiometry. We measure a metallicity of $\log_{10}[(\mathrm{M/H})/(\mathrm{M/H})_\star] = -0.09^{+0.66}_{-0.78}$ (or 0.1-3.7× stellar, 1σ). We adopt a stellar metallicity of $(\mathrm{M/H})_\star = 9.7 \times 10^{-4}$ (Brewer et al. 2016). Figure 5 shows that HD 209458 b sits just below the mass-metallicity relation for solar-system planets and other exoplanets with available measurements. In contrast to previous studies, the C/O and metallicity measurements presented here only depend on the parametrization chosen for the modeling, as no further assumption about the underlying elemental abundance ratios is made. However, we do implicitly assume that all the molecular species not included in our modeling have negligible abundances and do not influence the calculations.

5. ROBUSTNESS AGAINST THE CHOICE OF MOLECULAR LINE LIST DATABASES

The completeness and accuracy of molecular line list databases can influence the template-matching technique utilized for HDS studies (e.g., Hoeijmakers et al. 2015). In this context we explore the effect of two different line lists for water vapor on the outcome of our joint retrieval. We compare the Freedman et al. (2014) and the HITEMP2010 (Rothman et al. 2010) databases. On small wavelength ranges (10 nm), the two line lists produce models only mildly correlated (correlation of 0.35-0.4). Furthermore, their cross-correlation peaks a few km/s from zero lag, detectable at spectral resolutions above 2-3×10^4. It indicates a mismatch in both line position and line strength potentially affecting the measured planet radial velocity, line broadening, and significance of high-resolution models. This could bias measurements of mass and orbital inclination of non-transiting planets, planet rotation, and the current analysis.

We therefore also cross-correlate the HDS data with spectra produced with the HITEMP2010 database. When H_2O is mixed with the other species and over the full wavelength coverage of the CRIRES observations (2.27-2.35 μm) the agreement between the two analyses is remarkable, and we recover the same best-fitting values for absolute and relative molecular abundances. We measure a marginally lower significance of spectra produced with HITEMP2010, possibly due to the use of air pressure broadening versus the more appropriate H_2 broadening used for the Freedman database. Reconciling the disagreement observed on small wavelength ranges with the consistency of the full analysis presented here is not straightforward, and will be subject to future investigation.

6. CAVEATS AND FUTURE IMPROVEMENTS

As the first attempt at combining LDS and HDS, this study necessarily simplifies some details of the analysis. Firstly, the HDS analysis is conditioned on the posterior of the LDS analysis. Although this choice is consistent with our intent of computing a joint posterior distribution, it prevents us from exploring regions of the parameter space strongly disfavored by low-resolution spectra that could potentially be a good match to high-resolution spectra. Given the sample size of 5,000 points, we can reliably produce a joint posterior distribution for the 1-, 2- and 3-σ confidence intervals (right panels of Figure 2), with the least significant regions of the parameter space possibly affected by the sampling. In the future we will explore numerical algorithms capable of speeding up the comparison of model spectra to HDS data, so that a full MCMC on the latter will become feasible. In this way we will compute the LDS and

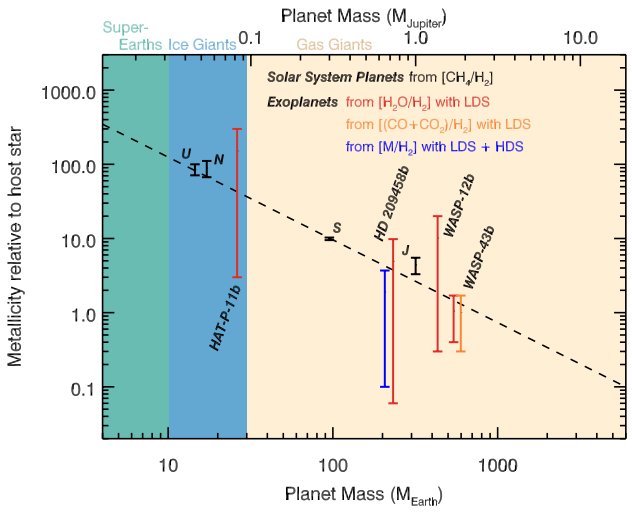

Figure 5. Measured metallicity of solar system planets (black error bars) and exoplanets with available measurements (colored error bars), as a function of mass. The value for HD 209458 b obtained here is shown in blue. Exoplanet data from Fraine et al. (2014); Kreidberg et al. (2014, 2015); Stevenson et al. (2016).

HDS posteriors independently, which will fully highlight the strengths and weaknesses of both datasets, and the power of combining them.

Another aspect that is worth mentioning is that in the current implementation we are equally weighting the HDS and LDS data. This is supported by the similar evidence for $CO+CO_2$ (4.1σ) and H_2O (6.2σ) reported in Line et al. (2016) and the detection of CO at S/N=5.2 in CRIRES data. Future work will be devoted to further assessing the relative weight of each dataset. This will enhance our predictive capabilities for designing coordinated observations with ground-based facilities and the James Webb Space Telescope.

Support for this work was provided by NASA through Hubble Fellowship grant HST-HF2-51336 awarded by the Space Telescope Science Institute, which is operated by the Association of Universities for Research in Astronomy, Inc., for NASA, under contract NAS5-26555. H. Schwarz acknowledges VICI grant 639.043.107, which is financed by The Netherlands Organisation for Scientific Research (NWO). We thank R. de Kok for useful discussion on the inaccuracies of molecular line lists and line-by-line radiative-transfer modeling. We thank C. Huitson and Z. Berta-Thompson for their insight into the joint posterior distribution of LDS and HDS data. We thank I. Snellen for his initial insight into the advantages of combining low- and high-resolution spectroscopy.

Facilities: HST(WFC3), Spitzer(IRAC), VLT(CRIRES)

REFERENCES

Benneke, B., & Seager, S. 2012, ApJ, 753, 100
Brewer, J. M., & Fischer, D. A. 2016, ApJ, 831, 20
Brewer, J. M., Fischer, D. A., Valenti, J. A., & Piskunov, N. 2016, ApJS, 225, 32
Brogi, M., Snellen, I. A. G., de Kok, R. J., et al. 2012, Nature, 486, 502
Brogi, M., de Kok, R. J., Birkby, J. L., et al. 2014, A&A, 565A, 124B
Brogi, M., de Kok, R. J., Albrecht, S., et al. 2016, ApJ, 817, 106
Charbonneau, D., Brown, T. M., Latham, D. W., & Mayor, M. 2000, ApJL, 529, 45
Diamond-Lowe, H., Stevenson, K. B., Bean, J. L. et al. 2014, ApJ, 796, 66
Evans, T. M., Aigrain, S., Gibson, N., et al. 2015, MNRAS, 451, 680
Fraine, J., Deming, D., Benneke, B., et al. 2014, Nature, 513, 526
Freedman, R. S., Marley, M. S., Lodders, K. 2008, ApJS, 174, 504
Freedman, R. S., Lustig-Yaeger, J., Fortney, J. J., et al. 2014, ApJS, 214, 25
Henry, G. W., Marcy, G. W., Butler, P. R., & Vogt, S. S. 2000, ApJL, 529, 41
Hoejimakers, H. J., de Kok, R. J., Snellen, I. A. G., et al. 2015, A&A, 575A, 20
Knutson, H. A., Charbonneau, D., Noyes, R. W., et al. 2007, ApJ, 655, 564
Knutson, H. A., Howard, A. W., & Isaacson, H. 2010, ApJ, 720, 1569
Knutson, H. A., Benneke, B., Deming, D., & Homeier, D. 2014, Nature, 505, 66
Kreidberg, L., Bean, J. L., Désert, J.-M., et al. 2014, Nature, 505, 69
Kreidberg, L., Line, M. R., Bean, J. L., et al. 2015, ApJ, 814, 66
Line, M. R., Knutson, H., Deming, D., et al. 2013, ApJ, 778, 183
Line, M. R., Knutson, H., Wolf, A. S., et al. 2014, ApJ, 783, 70
Line, M. R., Teske, J., Burningham, B., et al. 2015, ApJ, 807, 183
Line, M. R., Stevenson, K. B., Bean, J., et al. 2016, ApJ, accepted, 2016arXiv160508810L
Madhusudhan, N., & Seager, S. 2011, ApJ, 729, 41
Madhusudhan, N. 2012, ApJ, 758, 36
Parmentier, V., & Guillot, T. 2014, A&A, 562, A133
Rothman, L. S., Gordon, I. E., Barber, R. J., et al. 2010, JQSRT, 111, 2139
Schwarz, H., Brogi, M., de Kok, R., et al. 2015, A&A, 576A, 111
Sing, D. K., Fortney, J. J., Nikolov, N., et al. 2016, Nature, 529, 59
Snellen, I. A. G., de Kok, R. J., de Mooij, E. J. W., et al. 2010, Nature, 465, 1049
Snellen, I. A. G., Brandl, B. R., de Kok, R. J., et al. 2014, Nature, 509, 63S
Stevenson, K. B., Line, M. R., Bean, J. L., et al. 2016, arXiv:1608.00056
Torres, G., Winn, J. N., & Holman, M. J. 2008, ApJ, 677, 1324
Waldmann, I. P., Tinetti, G., Rocchetto, M., et al. 2015, ApJ, 802, 107